Tellus (1991), *43A*, 350–365

Mixed-layer dynamics and buoyancy transports

By MEHMET KARACA[1] and DETLEV MÜLLER[2], [1]*Boğaziçi University, Institute of Environmental Sciences, 80815 Bebek Istanbul, Turkey*; [2]*Space and Atmospheric Physics, Department of Physics, Imperial College, London SW7, UK*

(Manuscript received 4 May 1990; in final form 14 February 1991)

ABSTRACT

Ocean mixed layer (ML) dynamics are considered in the framework of a self-similar buoyancy profile governed by the Kraus-Turner budgets. The global validity of the profile is suggested by an inspection of Levitus-data. A parameterization of the mechanical energy forcing in terms of surface winds and heat fluxes is tested against weathership data in 1-dimensional (1D) model experiments. The ML-model is furthermore incorporated into a 3D transport-theory, where the consideration of 2 transport equations accounts for the Kraus–Turner concept. To test the transport theory, relative geostrophic velocities are derived from buoyancy-data. In addition to ML-dynamics, the empirical buoyancy-profile provides a convenient representation of this velocity field. For the mid-latitude Pacific, it is shown that these velocities, in conjunction with observed surface velocities, yield a realistic estimate of advective buoyancy-fluxes.

1. Introduction

The buoyancy-field of the upper ocean is determined by the interplay of local air-sea interactions and buoyancy-transports due to the large scale velocity-field. While advective fluxes play a minor role in midlatitudes, zonal buoyancy-transports by complex current systems are essential for the variability of the tropical ocean circulation on time-scales of several years. On longer time-scales, the poleward transport of equatorial buoyancy sets a decisive parameter for climatic conditions on the entire planet. In contrast to passive tracers, however, buoyancy is not only "shipped" by the velocity-field: buoyancy-gradients generate pressure-forces, which in turn drive the large-scale circulation. This paper discusses a model of the dynamics of the upper ocean buoyancy-field in view of the air-sea interaction and its coupling to the large scale velocity-field. The model is particularly designed for the implementation of a simple and yet sufficiently realistic form of ML-dynamics into current ocean circulation models (OCM).

For several weathership locations in the North-Atlantic it has been shown by the authors (Karaca and Müller, 1989, hereafter referred to as paper I) that the empirical assumption of a certain selfsimilar form of the buoyancy profile, governed by the Kraus–Turner budgets (Kraus and Turner, 1967), provides a realistic model for the vertical dynamics of the mixed-layer and the seasonal thermocline. To establish global validity for a phenomenological model of this type it would be desirable to derive the profile and its dynamics from an underlying theory. Unfortunately, contemporary turbulence theory is itself highly phenomenological and notorious for its lack of generality (Müller, 1987). The present paper confines itself therefore to an inspection of ocean-wide buoyancy data (Levitus, 1982), indeed suggesting the existence of a comparably simple, selfsimilar vertical structure of the ocean's buoyancy-field on a global scale.

Locally, Kraus–Turner models are forced by surface buoyancy-fluxes and the mechanical energy input. Currently available surface fluxes, observed or from atmospheric circulation models (ACM), yield sufficiently realistic simulations of ML-dynamics (Karaca and Müller, 1989), while an appropriate parameterization of the mechanical energy input is still under discussion. Here, a simple ansatz in the spirit of the original Kraus–Turner model will be considered. Using surface fluxes and winds from the UCLA-ACM, this parameterization is tested in 1D model experiments against weathership data.

Since the Kraus–Turner concept rests on the budgets of buoyancy and potential energy, the incorporation of ML-dynamics generally consider the buoyancy-equation only. The additionally necessary numerical expense can be partly reduced by integrating these equations in the vertical, thus obtaining a solely horizontal formulation of the transport problem. Due to the selfsimilarity of the profile, the vertical structure of the buoyancy-field is nevertheless fully retained in diagnostic form. The transport theory determines the buoyancy-distribution for given surface forcing and large-scale velocities. It is thus readily incorporated into an OCM, which provides the required velocity-field and calculates the buoyancy effects on these velocities.

OCM-experiments are not considered in the present paper. It will rather be shown that the buoyancy profile in addition to ML-dynamics admits a convenient representation of relative geostrophic velocities. Geostrophic velocity-fields are characteristic for the mid-latitude circulation away from boundary currents. Here, relative geostrophic velocities will be calculated for the mid-latitude Pacific with buoyancy profiles obtained from Levitus data. For the North Atlantic a similar investigation has been conducted by Olbers et al. (1985) and those concepts are essentially adopted here. Two differences should nevertheless be mentioned: for one, Olbers et al. do not use a buoyancy-profile, but derive velocities directly from (statistically processed) Levitus-data. Secondly, following Wunsch (1977) they employ an inverse β-spiral technique to determine absolute velocities. In the present paper, a simplified estimate of the absolute velocity-field is obtained by an appropriate combination of relative geostrophic velocities and observed surface velocities (Meehl, 1982). These velocities are inserted into the transport equations to derive a 1st order estimate of climatological features of advective buoyancy fluxes in the midlatitude Pacific. Data and model are regarded consistent, if these fluxes are sufficiently smaller than the surface forcing.

Different concepts of the combination of ML-dynamics and ocean circulation have been discussed in the literature. Rosati and Miyakoda (1988) couple a turbulence closure model of the ML with a velocity field governed by the primitive equations. Bleck et al. (1989) incorporate an elementary version of the Kraus–Turner model into an isopycnic circulation model. While the particular representation of the velocity-field is not crucial for the approach at hand, its specific features are twofold: the present version of the Kraus–Turner type ML-model includes thermocline-contributions to the buoyancy-budget of the upper ocean and, secondly, the entrainment-algorithm generally used is replaced by a second transport equation.

Model-experiments considered in this paper refer to a variety of data-sets from different sources.

(1) Surface fluxes and windstresses (AF): the atmospheric forcing used here is computed by the coarse version of the UCLA-ACM on a $4° \times 5°$ grid. Details of these model generated data and a comparison with observations are given in paper I.

(2) North Atlantic weathership data (WS): This data set, provided by the British Meteorological Office, represents 5-day averages of temperature-profiles, measured over a period of approximately 8 years. The profiles extend from the surface to a depth of 275 m. For the present purpose, average annual cycles have been derived from the original data for weatherships C(53° N, 35° W), D(44° N, 41° W), E(35° N, 48° W), J(52° N, 20° W) and K(45° N, 16° W). Further details of these data are discussed in paper I.

(3) Annually averaged global temperature fields (LA): These data have been published by S. Levitus (1982). The atlas provides annually averaged temperatures on a horizontal $1° \times 1°$ grid with 33 vertical levels extending from the surface to the bottom of the ocean.

(4) Monthly averaged temperature fields (LM): This Levitus (1982)-atlas represents monthly averaged global temperature-fields on a horizontal $1° \times 1°$ grid with 19 vertical levels extending from the surface to a depth of 1000 m. For the present purposes these data were averaged onto a horizontal $4° \times 5°$ grid for the Pacific between 50° N and 50° S.

(5) Seasonally averaged sea surface velocities (MV): This data set has been published by G. Meehl (1982), providing global sea surface velocities on a $5° \times 5°$ grid in 3-months intervals. For the present purposes these data were con-

verted onto a $4° \times 5°$ grid for the Pacific between 50° N and 50° S.

2. Mixed layer dynamics

For simplicity, the paper at hand considers buoyancy as a function of temperature only. Though buoyancy is basically proportional to heat in this case, the notion of buoyancy is preferred here, since ML-dynamics are primarily concerned with a fluid parcel's weight and potential energy and not so much with its internal energy, entropy and related thermodynamical problems. In practice, this restriction excludes high latitude oceans, where the vertical stability of the buoyancy-field is essentially maintained by salinity effects. Kraus–Turner type models of salinity dominated ML-dynamics have been extensively discussed by Lemke and coworkers (see for instance: Lemke and Manley, 1984).

It has been shown in paper I that WS-data are comprehensively represented by the assumption of a selfsimilar temperature profile for the upper ocean with the analytical form

$$T = \begin{cases} T_1 & 0 \geqslant z \geqslant -h_1 \\ T_0 + T_{10} e^D & -h_1 \geqslant z \geqslant -h_2, \end{cases} \tag{2.1}$$

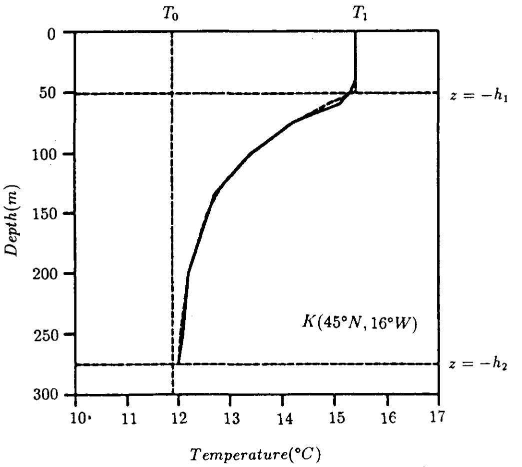

Fig. 1. Observed (solid line) and model (dashed line) profile at WSK for 4 November. Profile parameters are: $T_1 = 15.4°C$, $h_1 = 51$ m, $h_{12} = 63$ m, $T_b = 12°C$, $T_0 = 11.9°C$.

where T_1 denotes ML-temperature, h_1 the ML-depth, h_2 the total depth of the column, T_0 an asymptotic reference temperature and $T_{10} = T_1 - T_0$, while

$$D = (z + h_1)/h_{12},$$

where h_{12} is an exponential scale depth of the seasonal thermocline. With the bottom temperature $T_b = T(z = -h_2)$ and $T_{20} = T_b - T_0$, this scale depth always satisfies

$$h_{12} = (h_2 - h_1)/\theta,$$

where

$$\theta = \ln(T_{10}/T_{20}).$$

One such profile together with the corresponding observation from weathership K is shown in Fig. 1.

To envisage the limitations of the empirical expression (2.1), the model is compared to ocean-wide temperature observations. Fig. 2a shows temperature profiles from the LA-atlas for 3 latitudinal circles around the globe. Mixed layers are identified as "whiskers" at the top of the profiles. It is furthermore obvious that the exponential decrease of temperature beneath the ML captures the major features of the seasonal thermocline. At greater depth, generally somewhere between 1000 m and 2000 m, the profiles exhibit again a region of larger vertical gradients: the main thermocline. This feature is particularly pronounced in the Northeast Atlantic for the tongue of Mediterranean water in the vicinity of 36° N, while it is much less visible in the Pacific. These data indicate that the assumption of a selfsimilar profile can be extended into the deep ocean, representing the main thermocline by a second exponential.

Fig. 2b shows 3 meridional cross-sections through the world oceans from the LA-atlas. For low and medium latitudes the profiles exhibit similar features as in Fig. 2a. Poleward of about 60° latitude it is observed that cold ML-waters overlay warmer intermediate waters. As already mentioned, stability is ensured here by salinity effects. The seasonal thermocline retains nevertheless its exponential shape and the model (2.1) still applies with $T_1 < T_b < T_0$ in reversal of the corresponding inequality for lower latitudes.

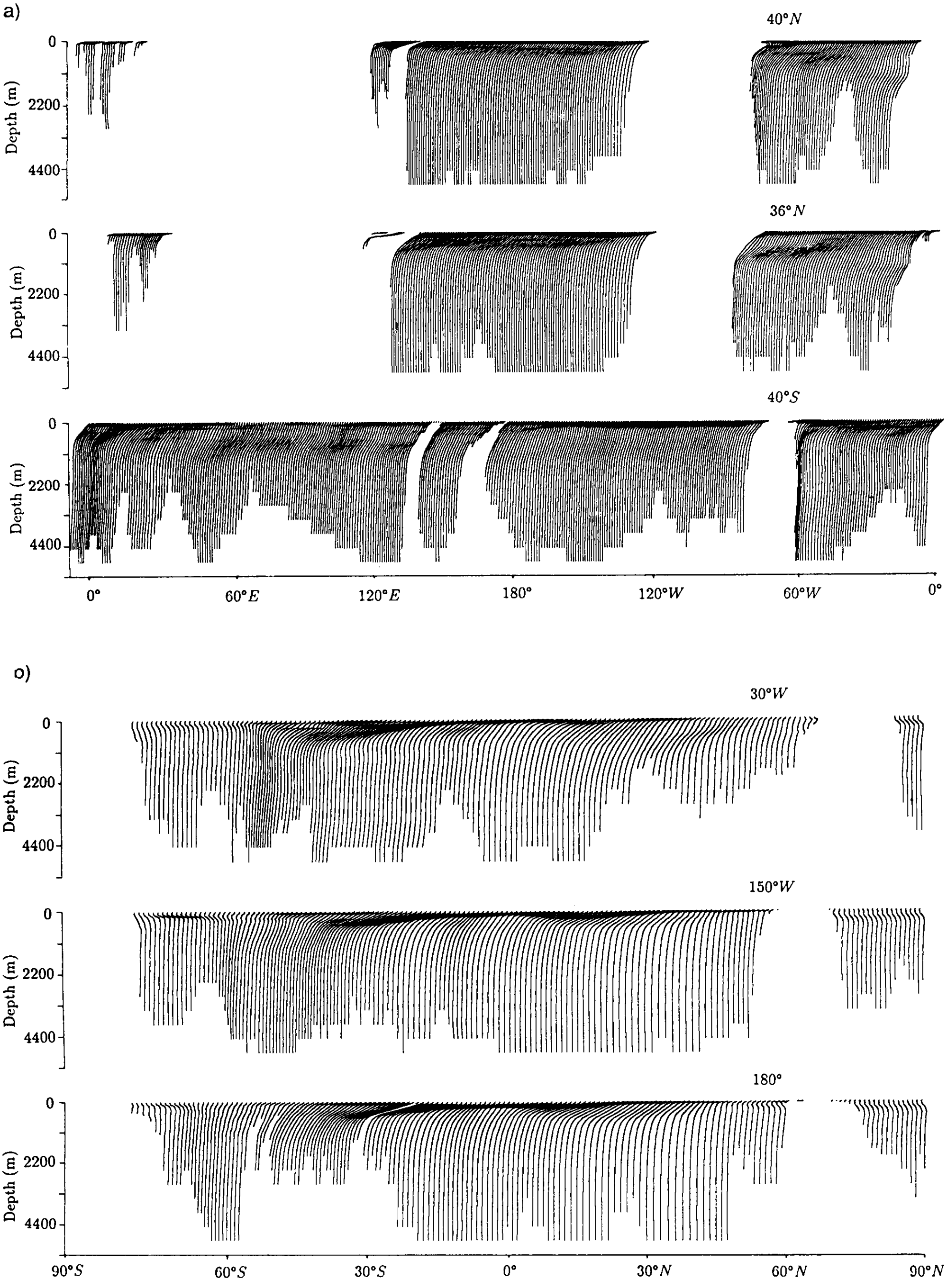

Fig. 2. Temperature profiles from the LA-atlas. (a) $T(\lambda, z)$ for 2 parallels in the Northern Hemisphere and 1 parallel in the Southern Hemisphere. The data show a pronounced main thermocline in the Eastern North Atlantic. (b) $T(\varphi, z)$ for the Atlantic (30° W) and the Pacific (150° W and 180). In high latitudes cold surface waters overlay warm deeper waters. A pronounced main thermocline is seen in the Atlantic approximately between 25° N and 40° N.

In a more rigorous comparison of model and data, the analytical expression (2.1) is fitted in a least square sense to LM-data in the Pacific between 50° N and 50° S. For this part of the upper and intermediate Pacific, polar effects and the main thermocline do not play a significant role so that (2.1) applies in its elementary form. The least-square procedure determines 12 monthly values for T_1, h_1, T_b and T_0 at each horizontal grid-point. In approximately 1% of the cases the LM-data reject the model (2.1) at a 95% significance level. Inspection of these rejects show that the exhibit pronounced warm or cold "noses" or steps, which are not confirmed by the neighbouring profiles. These cases are thus considered as data noise and the LM-profile is replaced by a linear interpolation from the generally 4 surrounding grid-points. For about 20% of the profiles a weak "dent" is observed well beneath the seasonal thermocline at depths between 600 m and 1000 m. Although the amplitude of these "dents" is much smaller than the seasonal thermocline or the main thermocline in the Atlantic, it can be speculated that this is the main thermocline in the Pacific, occurring at much lower depths and with much weaker amplitude than in the Atlantic. On the other hand, this phenomenon does not affect the model-significance at the 95% level, i.e., it cannot be significantly discriminated from noise in the framework of the present statistics. An ultimate interpretation requires the use of more extensive statistical methods as well as the inclusion of salinity-data. For the present purposes the "dents" are considered as insignificant data noise, accepting a possible loss of variability for intermediate waters. The results of the least-square fit indicate furthermore that the annual variability of T_b and T_0 at a given location does generally not exceed 1 $^\circ/_{oo}$. For simplicity, the 12 values of these temperatures at each location are replaced by their annual means so that the annual cycle of the temperature profile at a given grid point is determined by 12 values for T_1 and h_1 and the 2 constants T_b and T_0. ML-temperatures and depths for January are shown in Fig. 3 and for July in Fig. 4.

The figures show a pronounced seasonal signal in midlatitudes with warm and shallow MLs in the summer-hemisphere and cool and deeper MLs in the winter-hemisphere, while there is little seasonal variability near the equator. The surface temperatures exhibit a widely zonal pattern with maximum values in the Western Pacific. It is furthermore seen that the LM data represent the tropical Pacific with shallow and comparably cool ML in the East and deeper and warmer MLs in the West. These results coincide essentially with the current picture of the climatological features of the upper ocean buoyancy-field in the Pacific.

It can be concluded that the oceanic buoyancy-field exhibits indeed a globally selfsimilar vertical structure, which can be represented for the upper ocean by (2.1). Moreover, the model lends itself readily to generalizations, incorporating specific features of the polar oceans as well as the main thermocline.

The total buoyancy and potential energy of the

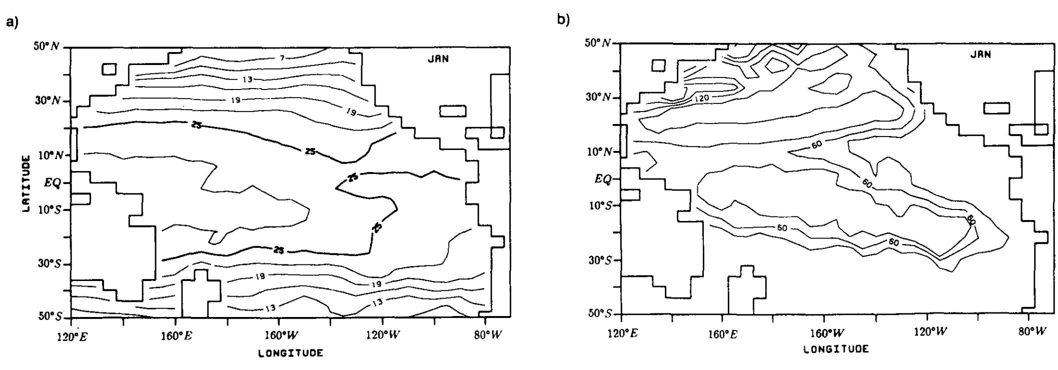

Fig. 3. Profile-parameters determined from LM-data for January. (a) ML-temperature T_1. Contour-interval 3°C. (b) ML-depth h_1. Contour-interval 30 m.

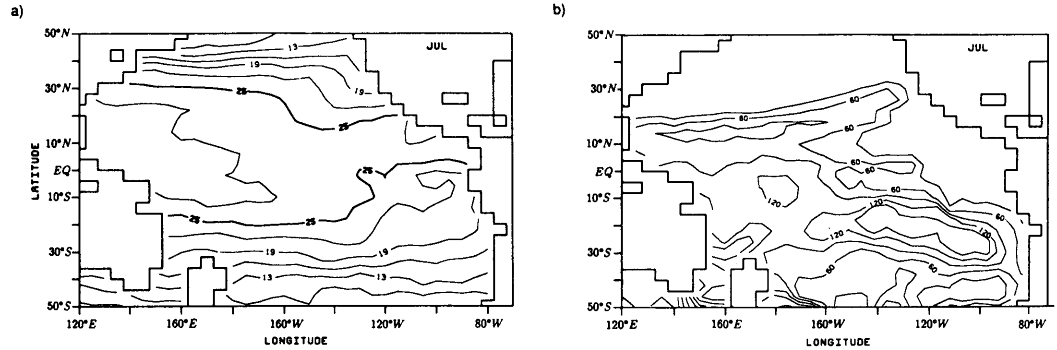

Fig. 4. Profile-parameters determined from LM-data for July. (a) ML-temperature T_1. (b) ML-depth h_1. Contour intervals as in Fig. 3.

column are now given by the zeroth and first moment of the temperature distribution:

$$R_N = \int_{-h_2}^{0} \mathrm{d}z (T - T_0)(-z)^N, \qquad N = 0, 1. \qquad (2.2.1)$$

It is convenient to introduce also the moments

$$S_N = \int_{-h_2}^{0} \mathrm{d}z (T - T_b)(-z)^N, \qquad (2.2.2)$$

which can be determined from data profiles independent of a specific hypothesis of the form (2.1), since they do not refer to an asymptotic temperature T_0. Inserting (2.1) into these integrals, one obtains

$$R_0 =: T_{10} h_q = T_{10} h_1 + (T_{10} - T_{20})\, h_{12}, \qquad (2.3.0)$$

$$R_1 =: R_0 h_p = \tfrac{1}{2} T_{10} h_1^2 + S_0 h_{12}, \qquad (2.3.1)$$

where h_q measures the thermal depth and h_p the depth of the center of gravity of the column. ML-dynamics follow now from the Kraus–Turner budgets

$$\dot{R}_0 = F_q, \qquad (2.4.0)$$

$$\dot{R}_1 = F_p, \qquad (2.4.1)$$

where F_q denotes the surface buoyancy-flux and F_p the mechanical energy input. To close the system, the boundary condition

$$T_{20} = T_{20}(t) \qquad (2.4.2)$$

has to be given at the system bottom. Insertion of (2.3) into (2.4) yields the dynamical equations for T_{10} and h_1. It may be noted that these equations (see paper I for details) exhibit highly nonlinear feedbacks. Extensive numerical studies have nevertheless indicated that for sufficiently realistic forcing the more or less trivial conditions: $T_{20} \leqslant T_{10}$ and $0 \leqslant h_1 \leqslant h_2$ seem to guarantee the existence of a unique solution.

Eqs. (2.4) are of course only meaningful, if a parameterization of the forcing-functions in terms of the state of the ocean and the atmosphere is available. For the winter season, AF-fluxes have been shown in paper I to provide a sufficiently realistic ML-forcing. This result will here be extended to the full annual cycle. To this end note that for the generally realistic condition $T_{20} = \text{const}$, equation (2.4.0) reduces to $\dot{S}_0 = F_q$, i.e.,

$$S_0(t) = S_0(t_0) + \int_{t_0}^{t} \mathrm{d}t' F_q(t'), \qquad (2.5.0)$$

while $S_0(t)$ can also be derived from WS-data according to (2.2.2). So the functions can be directly compared, determining the additive constant $S_0(t_0)$ by means of a least-square fit. For 5 weatherships this comparison is shown in Fig. 5a. Clearly in all cases both representations coincide satisfactorily with respect to phase and amplitude. It should be mentioned that similar calculations in paper I for the winter season alone also included the amplitude of the AF-fluxes into the statistical processing. In the present case of the full annual cycle, the additional tuning parameter has been completely dropped. Fig. 5a readily shows, why

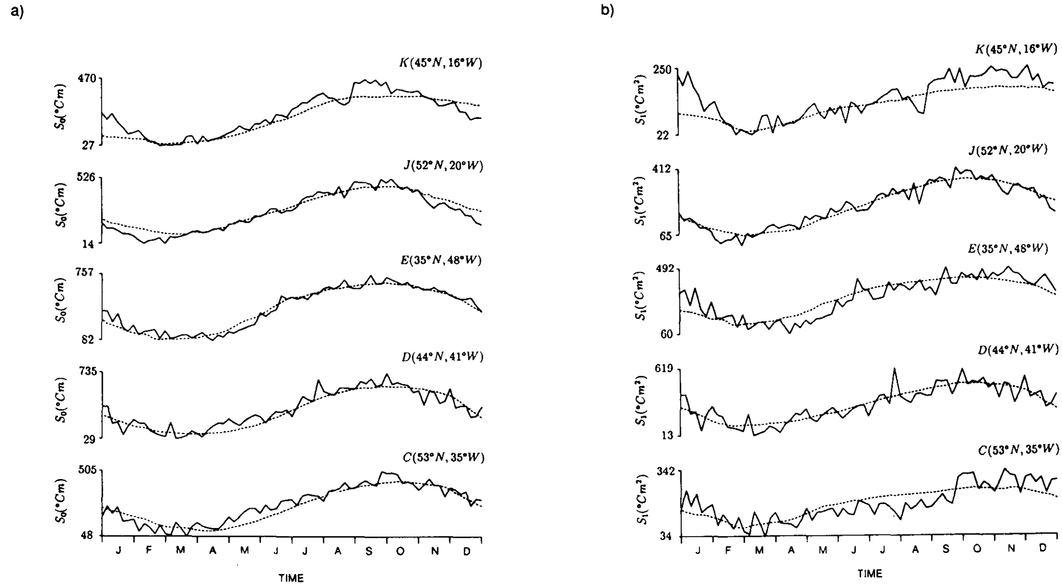

Fig. 5. Annual cycle in the upper ocean at 5 North Atlantic WS-stations. (a) Heat content S_0 (in °C m). Solid line: computed from temperature-data by (2.2.2). Dashed line: Computed from AF-fluxes by (2.5.0). (b) Potential energy S_1 (in 100°C m^2). Solid line: computed from temperature data by (2.2.2). Dashed line: Computed from AF-fluxes and winds by (2.5.1).

this is possible: during the winter season alone the signal-to-noise ratio in the WS-data is significantly worse than over the full annual cycle. Non-unity values of the amplitude fudge factor in these experiments account thus for relatively high noise-levels in the WS-data for the winter season alone and do in fact not criticize the AF-fluxes.

The characteristic problem of the F_p-parameterization is related to the transition from deep MLs at the end of winter to shallow MLs in early summer. It is the basic idea behind (2.4.1) that turbulent kinetic energy (TKE) performs the work necessary to lift heavy (cold) thermocline waters into the ML, leading to the h_1-increase observed throughout the major part of the year (Kraus and Turner, 1967). If spring is now conceived as a season of ML-"retreat", this argument no longer applies and (2.4.1) has to be suspended. For this period, the prognostic computation of h_1 is then generally replaced by the diagnostic Monin-Obukhov relation (Kraus and Turner, 1967).

On the other hand, it has been demonstrated in paper I that WS-data (still the qualitatively most consistent data of its kind) do not really show a period of well defined ML-"retreat". The data indicate rather that the ML-depth is subject to large fluctuations during spring, whose range is of the same order of magnitude as the system itself (see paper I, Fig. 5 and 6). A well-defined distinction between surface ML-waters and intermediate thermocline-waters is not really supported by the data for typical midlatitude spring conditions.

In fact, surface cooling and entrainment processes in the preceding winter have gradually transformed the ML-waters into intermediate waters and at some point this transformation was complete so that thermocline waters extend all the way to the surface. The ML-depth thus jumps more or less instantaneously from some maximum-value, which rarely exceeds 200 m in midlatitudes, to zero. In spring, TKE still mixes small amounts of light surface waters into a more or less homogeneous column, but the difference between "mixing" and "entrainment" becomes somewhat obscure. As a precursor of the systematic generation of new ML-waters, a buoyancy-gradient directly beneath the surface emerges and in early summer heating and well-defined entrainment recommence.

While this picture indeed restricts the existence of a differentiable or even continuous function $h_1(t)$ during the full annual cycle for midlatitudes, it is on the other hand well compatible with the validity of (2.4.1) throughout the whole year and this viewpoint will be adopted here. To obtain the F_p-parameterization note that (2.4.1) with (2.3.1) and (2.4.0) can be written as

$$F_p^* = \alpha g \left(\frac{1}{c_p} h_p F_q^* + \rho R_0 \dot{h}_p \right), \tag{2.6.0}$$

where

$$F_q^* = \rho c_p F_q, \qquad F_p^* = \alpha g \rho F_p,$$

where g denotes gravitational acceleration, α the coefficient of thermal expansion, c_p the heat capacity per unit mass and ρ the density of seawater. In the above expressions both, F_q^* and F_p^* have the dimension of W m^{-2}. The first term on the r.h.s. of (2.6.0) denotes the work necessary to distribute the buoyancy, supplied at the surface, over the whole system for fixed center of gravity. The second term describes the work necessary to dislocate the center of gravity, keeping the total buoyancy fixed. This dislocation is essentially a consequence of the entrainment-processes at the ML-base. According to Kraus and Turner (1967) this work is provided by the wind generated TKE, which can in turn be parameterized in terms of the atmospheric friction velocity u_*

$$\alpha g \rho R_0 \dot{h}_p = c \rho_A u_*^3,$$

where ρ_A is the density of air and c denotes the solely numerical drag coefficient of $O(10^{-3})$. Inserting this into (2.6.0) the mechanical energy input finally reads

$$F_p^* = c \rho_A u_*^3 + \frac{\alpha g}{c_p} h_p F_q^*. \tag{2.6.1}$$

This expression can again be tested using AF-fields for u_* and F_q and computing

$$S_1(t) = S_1(t_0) + \int_{t_0}^{t} dt' F_p(t'), \tag{2.5.1}$$

following from (2.4.1) for $T_{20} = \text{const}$. On the other hand, the same quantity is determined by (2.2.2) for WS-data. The comparison of the 2 functions at 5 WS-locations is shown in Fig. 5b, where the additive constant $S_1(t_0)$ has been determined in a least square sense and $c = 10^{-3}$ was used for all locations. Clearly, in all cases both representations coincide reasonably well with respect to phase and amplitude. The lack of specific discrepancies in spring confirms the use of (2.4.1) with (2.6.1) throughout the whole year. It is furthermore seen from Fig. 5 that the atmospheric forcing completely determines the buoyancy and potential energy budgets at all locations under consideration. Possible advective contributions cannot be meaningfully discriminated from noise. This is characteristic for midlatitude locations, where advection is too weak to affect the upper ocean buoyancy-field significantly on an annual timescale.

Finally, the model is integrated in time using AF-fluxes and windstresses as surface forcing and ignoring advection. For weathership E the results are shown in Fig. 6 and qualitatively similar results are obtained for the other weatherships. The integration procedure does not apply a time-stepping algorithm to the dynamical equations for T_{10} and h_1, but to the budgets (2.4). For constant lower boundary conditions (at WSE: $T_b = 17.1\,^\circ$C and $T_0 = 17.0\,^\circ$C) this is equivalent to (2.5). With

$$S_0 = R_0 - T_{20} h_2,$$
$$S_1 = R_1 - \tfrac{1}{2} T_{20} h_2^2,$$

it is now possible to iterate (2.3) numerically and thus compute T_1 and h_1 at every time-step. It is seen from Fig. 6 that the agreement of model and data is quite satisfactory. Initial values do generally not coincide, since $S_N(t_0)$ have been determined in a least square sense. As start values for the iteration procedure the T_1- and h_1-values of the former time-step are chosen and the procedure is terminated after 5 iterations for each time-step. During most of the year 3 iterations are completely sufficient, but in spring the convergence rate is clearly poorer. As discussed above the values of h_1 during this season have limited physical value. The fact that the variance of both h_1-curves in spring is comparable indicates first of all that the numerical noise in the least square fit of the WS-profiles and in the iteration procedure is of comparable order of magnitude. Notice furthermore that the winter values for h_1 remain within

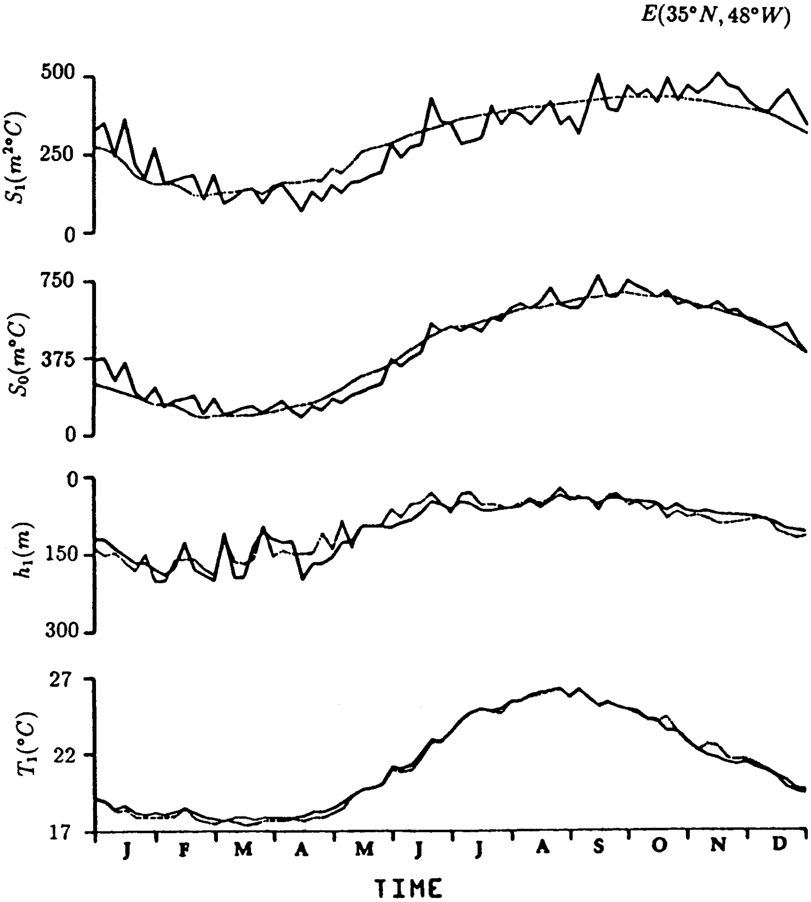

Fig. 6. 1-year integration of the 1D ML-model with AF-surface-forcing for WSE. Solid lines: WS-data, dotted lines: model forcing and results. T_1: ML-temperature (°C), h_1: ML-depth (m), S_0: heat-content (°C m), S_1: potential energy (°C m^2).

acceptable limits and the frequently obtained unrealistic deepening does not occur. This is essentially due to the fact that the parameterization (2.6.1), namely the second term on the r.h.s., provides the system with a sufficiently realistic loss of potential energy during the cooling period (see Fig. 5b). The significance of this effect has already been pointed out by Gill and Turner (1976). Its parameterization in (2.6.1) avoids in particular the introduction of additional tuning parameters.

3. Buoyancy transports

To minimize extensive tensor analytical formalism on the globe index notation will be used in the following, where the index v runs from 1 to 3, while the index n runs from 1 to 2. Representations in terms of the usual geophysical coordinates λ (longitude), φ (latitude) and z (depth) are obtained by setting

$$\partial^v = (\cos\varphi)^{-1} d^v,$$

where

$$d^v = [(a\cos\varphi)^{-2}\,\partial_\lambda,\, a^{-2}\,\partial_\varphi,\, \partial_z]$$

denotes the contravariant gradient vector with earth radius a and

$$v_v = w_v \cos\varphi,$$

where

$$w_v = (av_\lambda \cos\varphi, av_\varphi, v_z)$$

is the covariant velocity vector with physical velocities v_λ, v_φ, v_z of dimension ms^{-1}.

For the present purposes seawater is considered incompressible: $\rho = \mathrm{const}$, with buoyancy per unit mass (inertia)

$$b = -g[1 - \alpha(T - T_0)]. \quad (3.1.1)$$

The model is readily generalized to include salinity-effects in form of an additional linear term in (3.1.1). The incorporation of higher order terms in temperature and salinity is theoretically possible. In practice, however, this would lead to serious formal complications for the ML-model and the linearity of the buoyancy-relation is thus of some significance for the combination of ML-dynamics and buoyancy-transports, as discussed below. Each fluid parcel carries furthermore potential energy, which is defined per unit mass as

$$e_\mathrm{p} = -bz. \quad (3.1.2)$$

It should be emphasized that the buoyancy force cannot be obtained as the gradient of (3.1.2). The notion of "potential energy" is nevertheless retained, since the vertical integral of e_p provides a practical measure for the depth of the center of gravity in the water column (see eqs. (2.2.1) and (2.3.1)).

With (3.1) the fundamental budgets of mass, buoyancy and potential energy read

$$\partial^v v_v = 0, \quad (3.2.0)$$

$$\partial_t \rho b + \partial^v \rho b v_v = f_\mathrm{q}, \quad (3.2.1)$$

$$\partial_t \rho e_\mathrm{p} + \partial^v \rho e_\mathrm{p} v_v = f_\mathrm{p} - \rho b v_z. \quad (3.2.2)$$

Detailed properties of the local source functions f are irrelevant here, though it should be noted that f_p is essentially an abbreviation for the TKE-budget. It is a characteristic feature of these equations that both, (3.2.1) and (3.2.2) determine the same physical quantity, namely the temperature field. Independent information is nevertheless provided since both equations satisfy independent boundary condition.

Eqs. (3.2.1) and (3.2.2) can be cast into a strictly horizontal form by vertical integration. This will here be carried out under the assumptions that $v_z(z=0)=0$ and $v_z(z=-h_2)=0$, i.e., that in the midlatitude applications later up- and down-welling at the system bottom can be neglected. With these boundary conditions, one obtains

$$\partial_t R_0 + \partial^n R_0 V_n = F_\mathrm{q}, \quad (3.3.0)$$

$$\partial_t R_1 + \partial^n R_1 V_n + R_0 V_3 = F_\mathrm{p}, \quad (3.3.1)$$

where

$$F = (\alpha g \rho)^{-1} \int_{-h_2}^{0} \mathrm{d}z f$$

is equal to the surface forcing and the transport velocities V_n are defined by

$$R_0 V_n = \int_{-h_2}^{0} \mathrm{d}z (T - T_0)\, v_n. \quad (3.3.2)$$

The dependence of the vertical integral of the divergence-term in (3.2.2) on the profile moments and transport velocities can actually not be directly determined without knowledge of the vertical structure of the velocity field. The form (3.3.1), however, has to be generally valid and the quantity V_3 can be inferred from consistency requirements. To this end reconsider the 1D ML-model of section 2. Inserting (2.3.1) into (2.4) yields:

$$\dot{h}_\mathrm{p} = (F_\mathrm{p} - h_\mathrm{p} F_\mathrm{q})/R_0 =: F_\mathrm{m},$$

where F_m represents the mass-flux across the level $z = -h_\mathrm{p}$ as induced by the entrainment processes at the ML-base. In a 3D framework, this means that the surface $z = -h_\mathrm{p}(t, \lambda, \varphi)$ is not a material surface but

$$\partial_t h_\mathrm{p} + v_v(-h_\mathrm{p})\, \partial^v (h_\mathrm{p} + z) = F_\mathrm{m}.$$

Inserting this equation as well as (2.3.1) into (3.3.1) yields

$$V_3 = v_z(-h_\mathrm{p}) + (v_n(-h_\mathrm{p}) - V_n)\, \partial^n h_\mathrm{p}. \quad (3.3.3)$$

The system (3.3) determines R_0 and R_1 completely for given surface forcing and velocity field. It is emphasized that (3.3) is independent of any specific assumption on the buoyancy-profile. With (2.1), on the other hand, the vertical structure of the buoyancy field can be diagnostically obtained from (2.3) at each timestep, taking full account of the vertical ML-dynamics.

To test the transport theory, the knowledge of the velocity field is necessary. Here, relative geostrophic velocities in the midlatitude Pacific will be determined from LM-profiles. The combination of prognostic and advective buoyancy-transports with diagnostic, geostrophic velocities corresponds conceptually to large-scale geostrophic models of the ocean circulation (Hasselmann, 1982; Maier-Reimer and Hasselmann, 1987). These models utilize explicitly the pronounced time-scale separation between the slow buoyancy-field and the fast velocity-field, characterizing the bulk ocean circulation away from boundary currents and the equator.

For the North Atlantic, it has been shown by Olbers et al. (1985) that climatological features of the geostrophic velocity-field can be computed quite realistically from buoyancy-data. On the other hand, it has also been pointed out by those authors that due to the smoothing of the buoyancy data these velocities will generally not correspond to any actual state of the ocean circulation, even with the instantaneous eddy-field removed. Since climatological features of the advective buoyancy-fluxes are the interest at hand, this is not a grave limitation. It will be shown that the 4 profile parameters T_1, h_1, T_b and T_0, obtained in Section 2 from 19 LM-data at each grid point, completely determine the relative geostrophic velocities.

It should furthermore be emphasized that current OCMs model the buoyancy-feedback on the velocity-field in terms of far more complicated b(T)-relations than (3.1.1) (see for instance: Bryan and Cox, 1972, Unesco 1981). Since in practice, however, the Kraus–Turner concept of ML-dynamics is somewhat at odds with the introduction of higher order terms into (3.3.1), the simple linear form will here be retained for the determination of buoyancy-driven velocities.

Considering the absolute velocity v_n as the superposition

$$v_n = \phi_n + u_n, \tag{3.4.1}$$

where ϕ_n denotes barotropic and wind-driven contributions, one has from the hydrostatic and geostrophic relations

$$\partial_z u_n = f_{mn}\, \partial^m b$$

i.e.,

$$u_n = -f_{mn}\, \partial^m \int_z^0 \mathrm{d}rb, \tag{3.4.2}$$

for the buoyancy-driven component u_n relative to the surface. Here

$$f_{mn} = f_* \varepsilon_{mn}$$

with

$$f_* = \cos^2\varphi/(2\Omega \sin\varphi)$$

has been used and $\varepsilon_{11} = \varepsilon_{22} = 0$, while $\varepsilon_{12} = -\varepsilon_{21} = a^2 \cos\varphi$. With the profile (2.1) the integral in (3.4.2) can be carried out explicitly, yielding for the ML

$$u_n^1 = \alpha g z f_{mn}\, \partial^m T_{10}, \tag{3.5.1}$$

and the thermocline

$$u_n^2 = \alpha g f_{mn}\, \partial^m (R_0 + r_{02}), \tag{3.5.2}$$

where $r_{02} = (1 - \mathrm{e}^{\vartheta})\, T_{20} h_{12}$ and $\vartheta = (z + h_2)/h_{12}$. The corresponding vertical velocities follow from the continuity equation (3.2.0) as

$$u_z^1 = \tfrac{1}{2}\beta z^2\, \partial_\lambda T_{10}, \tag{3.6.1}$$

$$u_z^2 = -\beta\, \partial_\lambda (R_0 z + R_1 + r_{12}), \tag{3.6.2}$$

with $r_{12} = (T_{20}(h_2 + z) + r_{02})\, h_{12}$ and $\beta = \alpha g (2\Omega a^2 \sin^2\varphi)^{-1}$. By definition, these velocities vanish at the surface. Since according to (3.4.2) momentum-mixing in the ML is neglected, (3.5.1) is a linear function of depth. The velocities are furthermore continuous at the ML-base

$$u_n(-h_1) = \alpha g h_1 f_{mn}\, \partial^m T_{10},$$

$$u_z(-h_1) = \tfrac{1}{2}\beta h_1^2\, \partial_\lambda T_{10},$$

which is verified for (3.5.2) and (3.6.2) by differentiating first and then setting $z = -h_1$. At the bottom they assume the simple form:

$$u_n(-h_2) = \alpha g f_{nm}\, \partial^m R_0,$$

$$u_z(-h_2) = \beta\, \partial_\lambda (R_0 h_2 - R_1). \tag{3.7}$$

The above formulae give the relative geostrophic velocities as continuous profiles expressed in terms of horizontal gradients of the parameters and moments of the buoyancy-profile. These gradients can now be numerically computed for the LM-profiles. For the present, strictly diagnostic purposes it is sufficient to consider a non-staggered A-grid (Arakawa, 1972), carrying the buoyancy-field and its gradients at the same grid points. No assumptions are made on the boundary conditions for the velocity-field. The calculation of the velocity field rather shrinks the basin by 1 grid point from the continental boundaries and one additional grid point in the calculation of its divergence later on. Due to the break-down of (3.4.2) near the equator, an equatorial strip of 20° width is excluded from the computation, as well as regions of strong boundary-currents, where friction and/or nonlinearities invalidate the simple relation (3.4.2).

Profiles of relative geostrophic velocities, obtained from LM-buoyancy profiles by (3.5) are shown in Fig. 7. At the bottom ($z = -1000$ m) the

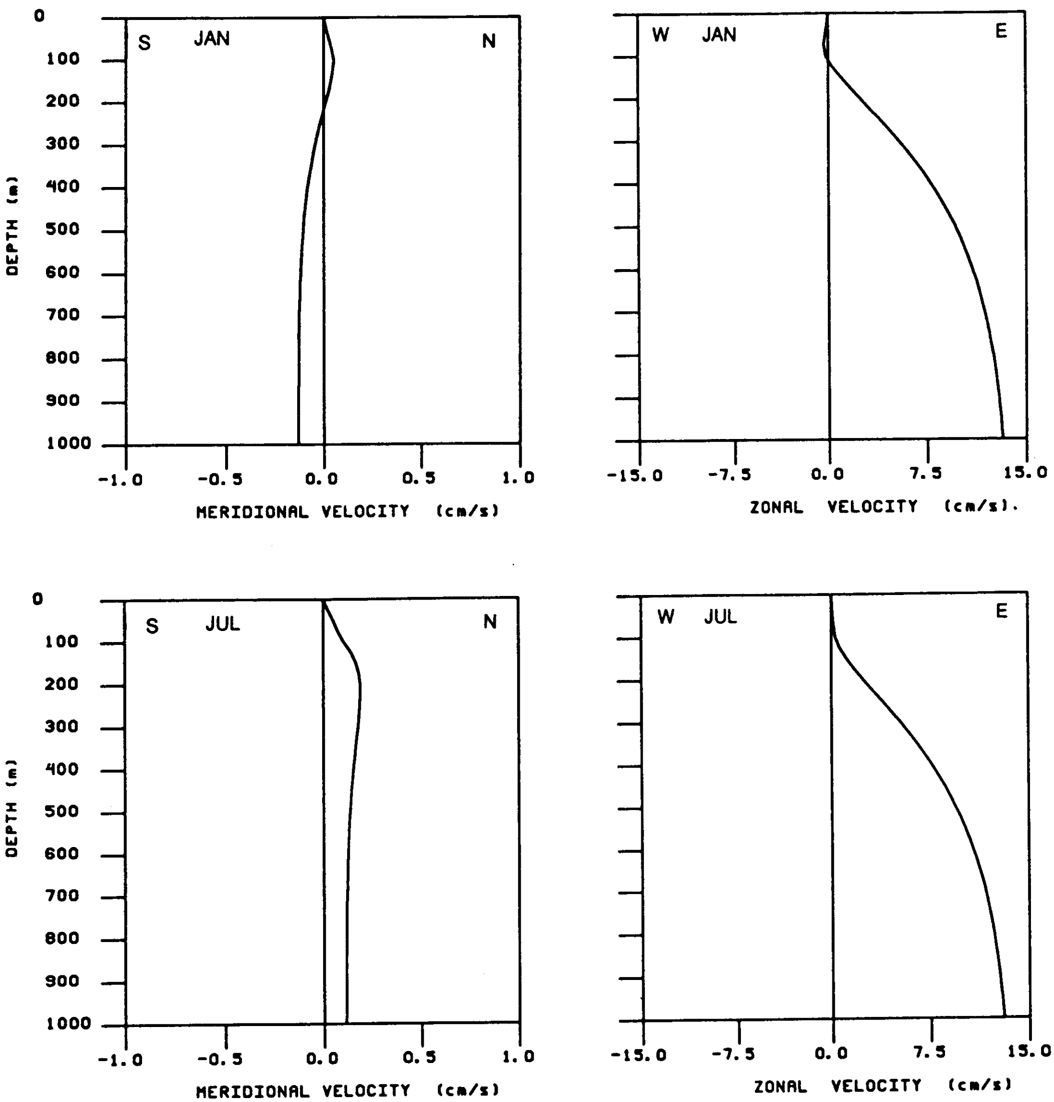

Fig. 7. Profiles of relative geostrophic velocities at 180, 18°N for January and July.

zonal component is seen to be about 13 cm s^{-1}. Basin-wide the bottom value of the zonal velocity ranges between 20 cm s^{-1} and 2 cm s^{-1}. The meridional velocity, on the other hand, assumes basin-wide values between 1 cm s^{-1} and 0.1 cm s^{-1} at the bottom. Major variations with depth occur in the upper part of the profile, in the thermocline directly beneath the ML. At this particular location the winter-profiles are seen to change sign with depth, while the summer profiles maintain the same direction over the whole column. However, this fact is of minor significance as long as the absolute values of the velocity are unknown.

Fig. 8 shows the basin-wide results for January at $z = -1000$ m. The figure displays a clear geostrophic response of the velocity-field to the subtropical warm water (i.e., low pressure) ponds with anticlockwise circulation in the Northern Hemisphere and clockwise circulation in the Southern Hemisphere. The major seasonal signal in this pattern is closely related to seasonal variations in the eastward extension of the warm waters. Thus the model captures the subtropical gyres as the dominant current system in the basin under consideration. Note that mass conservation for these relative velocities alone would require equatorward western boundary-currents. In comparison to results obtained by Olbers et al. (1985) for the North Atlantic, Fig. 8 exhibits a lesser degree of detail. This is not related to the use of the profile (2.1) in the present investigation. It is rather due to the coarse $4° \times 5°$ horizontal resolution of the buoyancy field chosen here in contrast to their $1° \times 1°$ resolution. The validity of (3.5) is essentially determined by the limitations of the geostrophic equilibrium assumption for the velocity-field. It may be noted again that the velocity field, as shown in Fig. 8, represents coarse climatological features and will generally not correspond to an instantaneous state of the ocean circulation.

To test the transport equations (3.3) the absolute velocity-field has to be known. This will

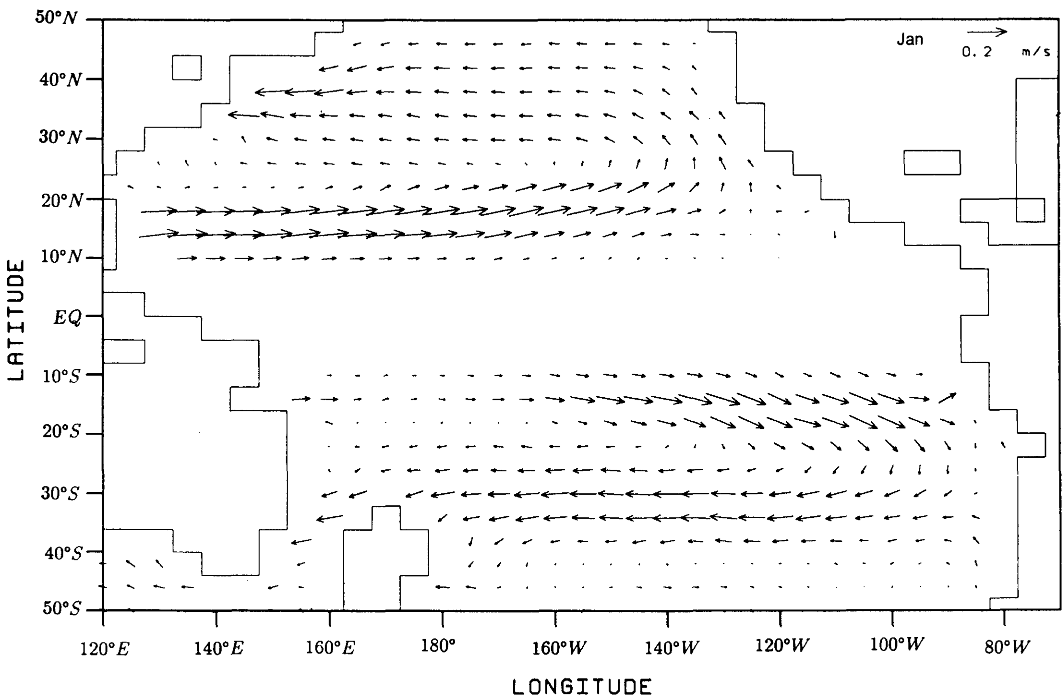

Fig. 8. Relative geostrophic velocities at $z = -1000$ m. The equatorial belt as well as regions near continental boundaries were excluded from the computation.

here be obtained by combining the relative velocities (3.5) with observed surface-velocities, as published by Meehl (1982). The MV-data are derived as long-term means from shipdrift observations and assume typical values of 10 cm s^{-1} to 30 cm s^{-1} in the Pacific domain under consideration. In the following they will be taken as the sum

$$\phi_n = u_n^0 + W_n \tag{3.8.1}$$

of the barotropic component u_n^0 and the surface value of the wind-driven component W_n. The computation of the transport velocities (3.3.2) with (3.4.1) has moreover to take into account that the wind-driven velocities do generally not penetrate to a depth of 1000 m. Thus, an estimate of the individual terms in (3.8.1) has to be given.

To this end it will here be assumed that

$$u_n^0 = -u_n(-h_2), \tag{3.8.2}$$

i.e., that for the present purposes the absolute velocity at $z = -1000$ m can be considered as zero. It has been pointed out by Kirwan et al. (1978) that buoy-derived velocities, which are comparable to shipdrift data (Meehl, 1982), are typically twice as large as geostrophic currents obtained from mean dynamic heights. For (3.8.2) not to be unrealistic this implies a relation

$$|\phi_n| \sim 2\,|u_n(-h_2)|$$

for the absolute values of the velocities, which is indeed approximately met by (3.7). It is furthermore seen from Fig. 7 that below 500 m the velocity profiles rapidly approach an asymptotic value, corresponding physically to the negative barotropic velocity. Olbers et al., on the other hand, show profiles of horizontal buoyancy-gradients, derived form LA-data, which do exhibit pronounced vertical variability in depths between 1000 m and 2000 m (see Fig. 5, Olbers et al., 1985). This indicates strongly against negligible absolute velocities in this depth range. They consider, however, a North Atlantic location (35° N, 25° W), which is well within the tongue of Mediterranean water, where a pronounced main thermocline at these depths provides an effective source of variability. This phenomenon is not observed in the Pacific (see Fig. 2a). Thus the estimate (3.8.2) will be assumed valid here and the geostrophic component of the transport velocity is computed according to

$$R_0 U_n = \int_{-h_2}^{0} \mathrm{d}z (T - T_0)(u_n + u_n^0), \tag{3.9.1}$$

where u_n is given by (3.5). It may be noted that (3.9.1) can be explicitly calculated in terms of horizontal gradients of R_1, R_0 and T_{20}, but the somewhat tedious algebra is of little value here and will therefore be omitted.

The surface value $w_n(z=0) = W_n$ of the wind-driven velocity is now obtained from the MV-data as

$$W_n = \phi_n + u_n(-h_2)$$

and it will be assumed that this velocity has a profile

$$w_n = W_n e^{z/h_1},$$

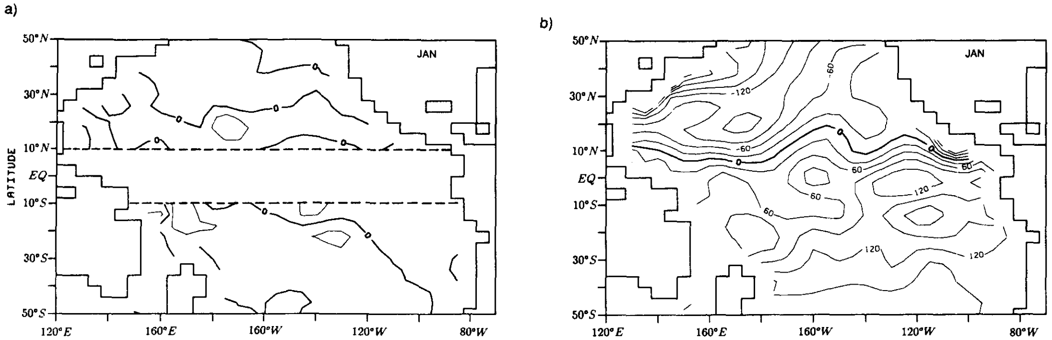

Fig. 9. Buoyancy fluxes (W m^{-2}) in the Pacific for January. (a) Advective fluxes (excluding the equatorial belt and continental boundaries). (b) AF-surface-fluxes. Contour-interval in both figures: 30 W m^{-2}.

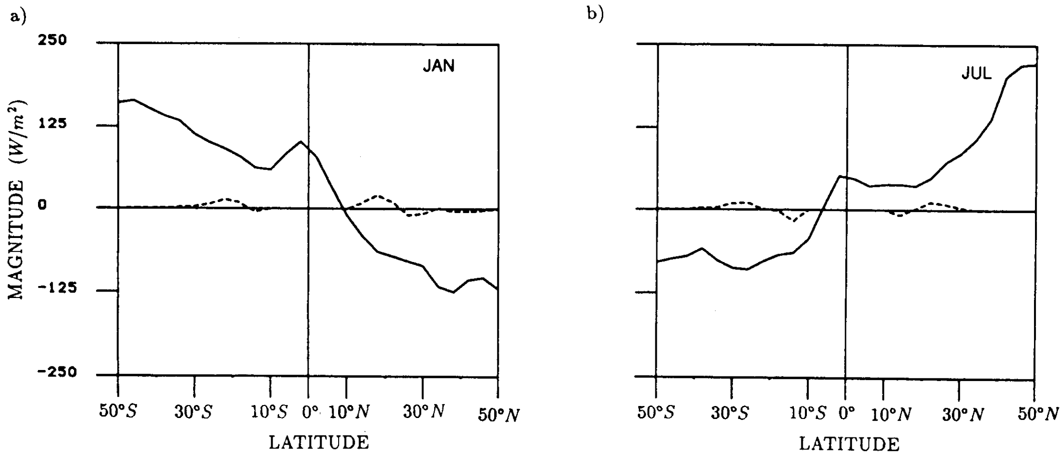

Fig. 10. Zonally averaged buoyancy-fluxes (W m^{-2}) in the Pacific for January and July. Solid line: AF-surface-fluxes. Dashed line: advective buoyancy flux excluding the equatorial belt and boundary currents.

where the ML-depth is used as an estimate for the scale depth of w_n. Though this may be somewhat large, it compares for midlatitudes to estimates of the Ekman-depth, given by Meehl (1982). The wind-driven contribution to the transport velocities is now calculated as

$$\int_{-h_1}^{0} \mathrm{d}z T_{10} w_n = 0.63 T_{10} h_1 W_n,$$

so that (3.3.2) finally becomes

$$R_0 V_n = R_0 U_n + 0.63 T_{10} h_1 W_n$$

and the advective buoyancy-flux F_A (in Wm^{-2}) is given as

$$F_A = -\rho c_p \partial^n R_0 V_n. \tag{3.10}$$

With LM-profiles and MV-data, this flux can now be directly calculated.

The results for January in comparison to AF-surface fluxes are shown in Fig. 9. Both panels employ the same contour-interval (30 Wm^{-2}) and it is seen that F_A barely exceed 30 Wm^{-2}, while F_q varies approximately between ± 150 Wm^{-2}. Fig. 10 compares the zonally averaged surface flux F_q with the zonally averaged advective flux F_A. Outside an equatorial belt the figure exhibit a difference of about one order of magnitude between the fluxes for both seasons. It should be emphasized that this relation will change, if the advection due to boundary currents is included. In the Southern Hemisphere, F_A shows little seasonal variability, while the advective fluxes in the Northern Hemisphere change sign between winter and summer. These results provide an independent confirmation of Fig. 5: the buoyancy-budget at midlatitude locations on an annual time-scale is to about 90% controlled by the surface forcing.

4. Conclusion

A review of ocean wide buoyancy data indicates that the vertical structure of the oceanic buoyancy field can be considered selfsimilar on a global scale. To first order, the data suggest essentially a 3-layer structure for all terrestrial oceans with surface ML, intermediate and deep waters. The analytic expression (2.1) representing the pronounced increase in weight per unit volume in the seasonal thermocline in terms of an exponential, captures the major features of observed profiles in surface and intermediate waters. Specific features of the polar ocean as well as the main thermocline can readily be incorporated into the model.

In the framework of a Kraus–Turner approach it is assumed that the potential energy budget of the upper ocean is essentially governed by the wind-generated TKE. A pronounced seasonal thermocline (i.e., a well-defined ML-depth) during most of the year enables a clear distinction between mixing and entrainment-effects of TKE.

In spring this is not the case. WS-data indicate however that a forcing parameterization, theoretically based on the entrainment effects of TKE, remains compatible with observed change-rates of potential energy during this season. A particular period of ML-"retreat" with suspension of the potential energy budget is not taken into account. The particular F_p-parameterization avoids moreover unrealistically deep ML during the winter season.

In this form, the Kraus–Turner budgets admit a straight forward incorporation of ML-dynamics into a transport scheme. Buoyancy transports in the upper ocean are consequently governed by 2 transport equations. For a simple linear $b(T)$-relation they assume the form of strictly horizontal budgets for the first moments of the profile. Together with the lower boundary condition, the moments uniquely determine the profile parameters and thus the complete vertical structure at each time-step.

The buoyancy-profile provides furthermore a concise representation for relative geostrophic velocities, if a linear $b(T)$ relation is used. For the midlatitude Pacific this velocity-field has been determined from LM-profiles with a horizontal resolution of $4° \times 5°$. With respect to pattern and magnitude the results yield a coarse picture of the baroclinic component of the subtropical gyre. The absolute velocity-field is obtained by combining relative geostrophic velocities with observed surface velocities. In the spirit of large-scale geostrophic models of the ocean-circulation the absolute velocities are incorporated into the transport equations. It is thus possible to calculate the advective buoyancy fluxes at a given location directly. Outside an equatorial belt and away from strong boundary currents the results for the Pacific show that the advective fluxes are generally one order of magnitude smaller than the surface forcing. This coincides with 1D ML-experiments based on WS-data and UCLA-ACM fluxes. For large parts of the terrestrial oceans, realistic simulations of sea surface temperatures should thus be feasible with the surface heat fluxes from a current atmospheric circulation model.

REFERENCES

Arakawa, A. 1972. Design of the UCLA General Circulation Model. Report No. 7, UCLA, Los Angeles, USA, 000 pp.

Bleck, R., Hanson, H. P., Hu, D. and Krauss, E. B. 1989. Mixed Layer Thermocline interaction in a three-dimensional isopycnic coordinate model. *J. Phys. Oceanogr. 19*, 1417–1439.

Bryan, K. and Cox, M. D. 1972. An approximate equation of state for numerical models of ocean circulation. *J. Phys. Oceanogr. 2*, 510–514.

Gill, A. and Turner, J. 1976. A comparison of seasonal thermocline models with observation. *Deep Sea Res. 23*, 391–401.

Hasselmann, K. 1982. An ocean model for climate variability studies. *Prog. Oceanogr. 11*, 69–62.

Karaca, M. and Müller, D. 1989. Simulation of sea-surface temperatures with surface heat fluxes from an atmospheric circulation model. *Tellus 41A*, 32–47.

Kirwan, A. D., McNally, G. J., Reynd, E. and Merrell Jr., W. J. 1978. The near surface circulation of the eastern north Pacific. *J. Phys. Oceanogr. 8*, 937–945.

Kraus, E. B. and Turner, J. 1967. A one-dimensional model of the seasonal thermocline. *Tellus 19*, 98–105.

Lemke, P. and Manley, T. 1984. The seasonal variation of the mixed-layer and the pycnocline under polar sea ice. *J. Geo. Res. 89*, 6494–6504.

Levitus, S. 1982. *Climatological atlas of the world ocean.* NOAA Prof. paper 13, Rockville, MD.

Maier-Reimer, E. and Hasselmann, K. 1987. Transport and storage of CO_2 in the ocean. An inorganic-ocean-circulation carbon cycle model. *Climate Dynamics 2*, 63–90.

Meehl, G. A. 1982. Characteristics of surface current flow inferred from a global ocean current data set. *J. Phys. Oceanogr. 12*, 538–555.

Müller, D. 1987. Turbulence and predictability in geophysical fluid dynamics and climate dynamics. *Internat. Agrophys. 3*, 77–91.

Olbers, D. J., Wenzel, M. and Willebrand, J. 1985. The inference of north Atlantic circulation patterns from climatological hydrographic data. *Rev. of Geophys. 23*, 313–356.

Rosati, A. and Miyakoda, K. 1988. A general circulation model for upper-ocean simulation. *J. Phys. Oceanogr. 18*, 1601–1626.

UNESCO, 1981. Tenth Report of the Joint Panel on Oceanographic Tables and Standards, Paris, 1981.

Wunsch, C. 1977. Determining the general circulation of the oceans: A preliminary discussion. *Science 196*, 871–875.